International Journal of Thermal Sciences 194 (2023) 108597

Contents lists available at ScienceDirect

International Journal of Thermal Sciences

journal homepage: www.elsevier.com/locate/ijts

Thermal stratification and self-pressurization in a cryogenic propellant storage tank considering capillary effect in low-gravity

Jicheng Li [a,e], Ziyi Guo [b,c], Yuan Zhang [d], Jianfu Zhao [b,c], Kai Li [b,c,*], Wenrui Hu [b,c]

[a] School of Energy and Power Engineering, Lanzhou University of Technology, Lanzhou, 730050, China
[b] National Microgravity Laboratory, Institute of Mechanics, Chinese Academy of Sciences, Beijing, 100190, China
[c] School of Engineering Science, University of Chinese Academy of Sciences, Beijing, 100049, China
[d] National Key Laboratory of Human Factors Engineering, China Astronaut Research and Training Center, Beijing, 100094, China
[e] Naipu Min Machinery Co Ltd, Shangrao, 334000, China

ARTICLE INFO

Keywords:
Thermal stratification
Self-pressurization
Heat and mass transfer
Storage tank
Low-gravity conditions
Two phase flow

ABSTRACT

Thermal stratification and self-pressurization in a propellant storage tank due to heat leakage from the wall are key issues of space fluid management. Under low-gravity conditions, the gas/liquid two-phase flow in a tank is complicated owing to the irregular interface morphology caused by the capillary effect. To clarify the heat and mass transfer process, the gas/liquid two-phase flow with the capillary effect accounted at the interface is systematically investigated by taking into account the volume of fluid (VOF) method for two-phase capturing and the Lee model for phase change. Spatial-temporal evolutions of thermal and pressure distributions and mass transfer rates at the interface in an axisymmetric scaling capsule tank of ethanol are studied depending on various gravity levels, liquid filling ratios, and boundary heat fluxes. The results show that the overall temperature, pressure, and thermal distributions inside the tank are significantly affected by the gravity level, liquid filling ratio, and boundary heat flux, while the pressure distributions are quite similar under different conditions. The influence of gravity levels mainly originated from various interface configurations due to the capillary effect. Therefore, the capillary effect plays an important role in the heat and mass transfer process in low-gravity environments.

1. Introduction

Cryogenic propellant plays a key role in energy system in space. However, it is sensitive to the heat leakage from space environment due to its low boiling point. In a partially filled propellant tank, the phenomenon of gas/liquid two-phase flow inside the tank is complicated under microgravity condition. Capillary force becomes the major factor, resulting in an uneven distribution of two-phase flow field and irregular interface morphology. Moreover, when encounters local heat leakage on the wall of the propellant tank, temperature stratification arises around the heat leakage source. This will lead to local overheating, and will also seriously affect the multiphase heat and mass transfer in the propellant tank, thereby raising the pressure inside the tank and endangering the structural safety of the system. Therefore, thermal stratification and self-pressurization in a cryogenic propellant storage tank caused by heat leakage from the wall of the tank are key issues of space fluid management (SFM).

The cost of space experiments on the propellant tank is tremendously high. Hence, thermal stratification and self-pressurization in storage tanks were mainly studied by terrestrial experiments and theoretical analyses at the early stage. Schmidt et al. [1] carried out on-ground experiments in a Dewar bottle of 625 gallons in volume. The thermal fields were measured for various pressure levels, pressurization gas consumptions and ullage pressure, and a thermodynamic analysis method was applied to investigate the mechanism of heat transfer and thermal desorption in a liquid hydrogen (LH_2) storage tank. Barnett et al. [2] adopted a semi-empirical method to analyze the convective boundary layer and the observed hyperbolic temperature profile distribution, and predict the thermal distribution in the tank. Aydelott et al. [3–5] carried out experimental investigations on a spherical LH_2 storage tank under gravitational conditions. Influences of liquid filling ratio, heat transfer rate, heat leakage position, and tank size on the pressurization rate were analyzed. The results showed that the pressurization rate was mainly affected by the heat leakage position. Their further study conducted under microgravity condition indicated that the

* Corresponding author. National Microgravity Laboratory, Institute of Mechanics, Chinese Academy of Sciences, Beijing, 100190, China.
E-mail address: likai@imech.ac.cn (K. Li).

https://doi.org/10.1016/j.ijthermalsci.2023.108597
Received 15 March 2023; Received in revised form 28 July 2023; Accepted 10 August 2023
Available online 27 August 2023

Nomenclature

C	coefficient of Lee model, s^{-1}
c_p	specific heat at constant pressure, kJ/(kg·K)
c_v	specific heat at constant volume, kJ/(kg·K)
E	energy, J/kg
$\boldsymbol{F}_M$	body force of surface tension, kg/(m·s)^2
$\boldsymbol{g}$	gravity vector, m/s^2
g_0	terrestrial gravitational acceleration, m/s^2
h	heat transfer coefficient, W/(m^2·K)
H	height of the tank, m
Δh	latent heat, J/kg
k	thermal conductivity, W/(m·K)
Ma	Marangoni number
$\widehat{\boldsymbol{n}}$	unit normal vector
Nu	Nusselt number
p	pressure, Pa or kPa
Pr	Prandtl number
q''	heat flux, W/m^2
R	radius of the tank, m
S_h	Energy source term, J/kg
Ra	Rayleigh number
Re	Reynolds number
S_m	mass source term, kg/(m^3·s)
T	temperature, K
$\widehat{\boldsymbol{t}}$	tangential vector
$\boldsymbol{u}$	velocity vector, m/s
$\boldsymbol{x}$	position vector, (x, y, z)

Greek symbols

α	volume fraction
β	thermal expansion coefficient, K^{-1}
κ	curvature of interface, 1/m
ℓ	characteristic length, m
λ	thermal diffusivity, m^2/s
ρ	density, kg/m^3
σ	surface tension coefficient, N/m or mN/m
θ	contact angle, rad
μ	dynamic viscosity, Pa·s
χ	slip length, m
Ω	computational domain
∇	Laplacian operator

Subscripts

0	initial time condition
g	vapor
l	liquid
w	wall boundary

Abbreviations

AMR	adaptive mesh refinement
VOF	volume of fluid

pressurization rate was lower than that under terrestrial gravity due to the increase of wet wall area and the enhancement of vaporization. Hasan et al. [6] experimentally studied the thermal stratification and self-pressurization in LH_2 storage tanks under terrestrial gravity. Their results showed that with the increase of heat flux, the pressurization rate increased and the thermal stratification became severer. Lin and Hasan [7] theoretically studied thermal stratification and self-pressurization in a spherical LH_2 storage tank under microgravity. Using a simplified one-dimensional (1D) model with certain assumptions, such as uniform temperature in ullage, compressible and motionless liquid, and effects of the size of tank, they studied the influences of liquid filling ratio and wall heat flux on the thermal stratification and self-pressurization. They claimed that the thermal expansion of liquid caused the condensation of vapor, and the wall heat flux led to the evaporation of liquid at the interface. The combined effect of the liquid filling ratio and the wall heat flux determined the direction of mass transfer at the gas/liquid interface (noted as interface hereafter).

With the development of Computational Fluid Dynamics (CFD), more accurate and sophisticated numerical studies on the phenomena of thermal stratification and self-pressurization in propellant storage tanks have become a hotspot. Hochstein et al. [8] studied the pressurization control with software SOLA-ECLIPSE, and compared with the experimental results obtained by Aydelott [4,5] on the influence of heating mode, tank size and gravity, respectively. Later, they conducted numerical studies on the influence of super-cooling on the pressurization rate in full-size on-orbit storage tanks [9]. Their results showed that even a small amount of super-cooling could significantly reduce the rate of self-pressurization. Grayson et al. [10] numerically studied self-pressurization by external heating and decompression by thermodynamic exhaust under normal gravitational conditions. It is assumed that the liquid phase is incompressible and its density is only a function of temperature. The corresponding pressure and temperature predictions were in good agreement with the experimental results given by sensor measurements. Barsi and Kassemi [11] proposed a two-phase CFD model to describe the self-pressurization behavior in a partially filled LH_2 storage tank under normal gravity. The predictive ability of the model was verified by experiments for various liquid filling ratios. Later, they studied thermal stratification and self-pressurization with different heat flux boundary conditions in a scaling model tank in ground experiments [12] and numerical simulations [13]. Chen et al. [14] and Kartuzova et al. [15] established a numerical simulation method for thermal stratification and self-pressurization in a large-scale storage tank in terrestrial conditions, and the temporal evolutions of pressure inside the tank were studied ignoring the surface tension (capillary effects). Afterward, Kassemi et al. [16] investigated the influence of turbulent model on the heat and mass transfer rate, and analyzed the effectiveness of using laminar and turbulent models to predict the heat transfer and self-pressurization with phase transition in the tank. In the follow-up research, they also conducted a space microgravity experiment on a small-scale model tank (Tank Pressure Control Experiment) to investigate the effect of gravitational acceleration on phase transition and mass transfer [17]. It is found that the existing numerical model could simulate the dynamic evolutions of the pressure inside the tank better in microgravity condition. They also adopted the flat liquid surface assumption (i.e. the capillary climbing effect was ignored). Liu et al. [18,19] studied the thermal stratification in a liquid hydrogen tank under various gravity conditions, and the thermal protection of tanks on the ground and during the launching process was also investigated [20]. Wang et al. [21] studied the thermodynamic characteristics of LH_2 storage tanks under various gravity conditions. In addition, Xie et al. [22] tried to suppress self-pressurization in a liquid hydrogen tank by injecting helium into the tank. Liu et al. [23] also studied the thermodynamic characteristics of the mixture of liquid oxygen and helium in a tank.

Mathematical models on the self-pressurization process were widely studied at the same time, such as the lumped model concerning the temperature gradient in both the vapor and liquid phase [24], the influence of various gravity levels on thermal stratification in cryogenic propellant tanks [25], the evaporation-condensation in the active pressure control process [26], the optimized transient model for the self-pressurization process [27], and the orthogonal experiments and lumped steam models for the self-pressurization and thermodynamic

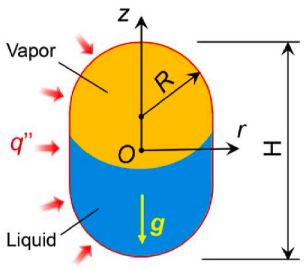

Fig. 1. Sketch of the axisymmetric scaling capsule tank.

Table 1
Properties of liquid (first line) and vapor (second line) ethanol at different temperature *T*. Linear interpolation method is used for the detailed value of these properties in numerical simulation except for the density of vapor.

T	*p*	*ρ*	c_v	c_p	*μ*	*k*
K	MPa	kg/m^3	kJ/(kg·K)	kJ/(kg·K)	μPa·s	mW/(m·K)
340	0.06303	747.6	2.350	2.812	524.3	155.5
340	0.06303	1.052	1.428	1.645	10.04	20.97
360	0.1400	727.9	2.497	3.023	389.6	151.4
360	0.1400	2.245	1.532	1.778	10.63	22.84
380	0.2821	706.4	2.639	3.257	296.0	147.2
380	0.2821	4.393	1.651	1.943	11.22	25.04
400	0.5237	682.1	2.771	3.516	228.1	143.0
400	0.5237	8.010	1.786	2.150	11.82	27.75
420	0.9064	654.2	2.880	3.790	177.1	138.5
420	0.9064	13.80	1.938	2.418	12.44	31.24
440	1.478	621.8	2.961	4.060	137.9	134.0
440	1.478	22.77	2.111	2.785	13.13	36.00
460	2.289	583.9	3.027	4.365	107.6	130.0
460	2.289	36.47	2.308	3.339	13.96	42.94
480	3.398	537.8	3.113	4.959	83.55	127.4
480	3.398	57.90	2.544	4.381	15.11	54.07
500	4.872	467.4	3.273	7.648	60.98	129.7
500	4.872	96.62	2.866	8.052	17.23	76.63

vent process in a cryogenic tank [28]. Lv et al. [29] also conducted thermodynamic analyses on the effect of tank size in the self-pressurization process and found that the size effect disappeared when the tank size exceeded a threshold. These mathematical and physical models mainly depend on the selection of specific parameters. However, the accuracy of simulation about self-pressurization and thermodynamic process in cryogenic propellant tanks still needs to be improved.

Therefore, the thermal stratification and self-pressurization process in a propellant storage tank in low-gravity environment remains an open problem. Note that most of the aforementioned studies assumed a planar interface, without considering the capillary climbing effect. However, this kind of planar interface assumption is always invalid in low-gravity conditions. Due to the significant difference between liquid and vapor in terms of heat capacity, the gas/liquid phase distribution inside the tank plays a key role in the heat and mass transfer process. As a result, the curved interface may cause diversities of the spatial-temporal evolutions of thermal and pressure distributions in a tank. In addition, we adopt ethanol as a promising liquid propellant besides the commonly used LH_2 and liquid oxygen (LO_2) in this study. It has advantages in the applications in spacecraft which do not require particularly high thrust. For example, ethanol was used in early RS-88 engines (ethanol/liquid oxygen as propellant) [30], sounding rockets [31], and as a propellant for the re-supplement of satellites.

In the present study, on the basis of considering the capillary effect in a scaling capsule tank under low-gravity condition, we systematically investigate the thermal stratification and self-pressurization process in the tank depending on various gravity levels, liquid filling ratios, and boundary heat fluxes. The widely used VOF method for two phase capture and the Lee model for phase change were adopted and validated. This research reveals the spatial-temporal evolutions of thermal and pressure distributions, and further investigates the heat and mass transfer process in a tank. It provides an effective research method for the phase change and heat and mass transfer process in space containers and systems in low-gravity environment.

2. Physical and mathematical models

An axisymmetric scaling capsule tank, two hemispheres of the same radius connected with a straight cylinder, is sketched in Fig. 1. The radii of the cylinder and the hemispheres are $R = 35$ mm, and the total height of the tank is $H = 105$ mm. A cylindrical coordinate system (r, θ, z) is adopted with the origin O located at the center of the symmetric axis center. The gravity is downward in the z-direction. The working medium is liquid ethanol (C_2H_5OH) and its vapor. Heat leakage occurs on the wall of the tank with the heat flux of q''.

Assumptions are adopted in the description of the physical model. Thermophysical properties of the two-phase system (see Table 1) are in the form of $X = \alpha_l X_l + (1 - \alpha_l)X_g$, where X is the thermophysical property, such as k, μ, ρ, and α is the volume fraction. The subscripts l and g stand for liquid and vapor phases. The Boussinesq assumption is adopted for the liquid phase, and the vapor phase is assumed as ideal gas. The mass and energy change induced by phase change are considered, while the momentum change is ignored. Since the superheat of liquid near the tank wall in the present study is generally less than 5 K, the effect of boiling on the wall is not taken into consideration. The phase change only occurs at the interface when the temperature reaches its saturation value at the corresponding pressure. The interface is assumed in a quasi-equilibrium state in the process of phase change.

The governing equations are as follows.

Continuity equation:

$$\frac{\partial \rho}{\partial t} + \nabla \cdot (\rho \boldsymbol{u}) = 0 \tag{1}$$

Momentum equation:

$$\frac{\partial (\rho \boldsymbol{u})}{\partial t} + \nabla \cdot (\rho \boldsymbol{u}\boldsymbol{u}) = -\nabla p + \nabla \cdot \left[\mu\left(\nabla \boldsymbol{u} + \nabla \boldsymbol{u}^T\right)\right] + \rho \boldsymbol{g} + \boldsymbol{F}_M \tag{2}$$

where the momentum source term $\boldsymbol{F}_M$ stands for the contribution of surface tension, and the continuum surface force (CSF) model [32] is used, in which the surface tension effect is given by a step body force term

$$\boldsymbol{F}_M = \sigma \frac{\rho \kappa_g \nabla \alpha_g}{\frac{1}{2}\left(\rho_g + \rho_l\right)} \tag{3}$$

where the curvature $\kappa = -\nabla \cdot \hat{\boldsymbol{n}}$, and the normal vector $\hat{\boldsymbol{n}} = \nabla\alpha / \|\nabla\alpha\|$. The surface tension coefficient σ is assumed as a linear function of the temperature, i.e., $\sigma = 24.05–0.0832\ (T - 273.15)$ mN/m [33].

Energy equation:

$$\frac{\partial}{\partial t}(\rho E) + \nabla \cdot (\boldsymbol{u}(\rho E + p)) = \nabla \cdot (k \nabla T) + S_h \tag{4}$$

where the energy $E = e + u^2/2$ and the inner energy $e = c_v T$. The heat source term S_h can be calculated by $S_h = S_m \cdot \Delta h$, where the latent heat Δh is (obtained from NIST) given by

$$\Delta h = \Delta_{vap} H = A \exp(-\alpha T_r)\ (1 - T_r)^{\beta_2} \tag{5}$$

where $T_r = T/T_c$ and $T_c = 513.9$ K, $A = 50.43$ kJ/mol, $\alpha = -0.4475$, $\beta_2 = 0.4989$.

No-slip and non-penetrating boundary conditions are adopted for the velocity at the tank wall, excepting for the moving contact line region (i.e. triple-phase contact line region) where the Navier-slip boundary condition

$$u_{\parallel} = \chi \hat{\boldsymbol{n}}_w \cdot \nabla u_{\parallel} \tag{6}$$

is considered. The $u_{\parallel}$ is the tangent velocity parallel to the wall, $\hat{\boldsymbol{n}}_w$ is the unit vector normal to the wall. χ is the slip length and is selected as 10^{-6} m according to Hoffman's experiment [34], which has the same order of the height of the first grid layer on the wall. The boundary conditions for pressure p and volume fraction α at the wall of the tank are

$$\left.\frac{\partial p}{\partial n}\right|_w = 0, \left.\frac{\partial \alpha}{\partial n}\right|_w = 0 \tag{7}$$

The effect of the contact angle is described in the wall adhesion model given by [32].

$$\hat{\boldsymbol{n}} = \hat{\boldsymbol{n}}_w \cos\theta_w + \hat{\boldsymbol{t}}_w \sin\theta_w \tag{8}$$

where $\hat{\boldsymbol{t}}_w$ is the unit vector tangential to the wall and θ_w is the static contact angle. The heat flux boundary condition is applied on the wall of the tank,

$$q'' = -k\frac{\partial T}{\partial n} \tag{9}$$

where q'' is selected as 5 W/m^2, 50 W/m^2 and 100 W/m^2, respectively.

In the present study, the heat and mass transfer inside the tank is dominated by natural convection driven by buoyancy and thermocapillary effect under low-gravity condition. Dimensional analysis indicates that the flows in the tank are determined by Rayleigh number (Ra), Prandtl number (Pr) and Marangoni number (Ma), defined by

$$Ra = \frac{\rho g \beta \Delta T \ell^3}{\mu\lambda} \tag{10}$$

$$Pr = \nu/\lambda \tag{11}$$

and

$$Ma = \frac{|\sigma_T|\Delta T \ell}{\mu\lambda} \tag{12}$$

where ℓ is the characteristic length of the tank ($\ell = R = 35$ mm), λ is thermal diffusivity, $\lambda = k/\rho c_p$, and σ_T is temperature coefficient of the surface tension, $\sigma_T = \partial\sigma/\partial T$. The thermal expansion coefficient $\beta = 0.001353$ K^{-1}. The characteristic velocity of buoyancy convection near the tank wall is given by [35]

$$u_z \sim \rho g \beta \Delta T \ell^2/\mu \tag{13}$$

and the characteristic velocity of the thermocapillary convection by

$$u_c \sim \sigma_T \Delta T/\mu \tag{14}$$

For the present scaling tank of ethanol under $10^{-2}g_0$ gravity, the corresponding Reynolds number $Re = \rho u \ell/\mu = 26.3 \sim 262.7$. Therefore, the flow inside the tank is assumed to be laminar. The initial velocity, pressure and temperature inside the tank are 0 m/s, 10^5Pa and 351.12 K, respectively.

3. Numerical methods and validations

The Volume of Fluid (VOF) method [36,37] is adopted to capture the interface in the tank, and this method has been validated in Refs. [38, 39]. The governing equation of VOF is given by

$$\frac{\partial}{\partial t}(\alpha_l \rho_l) + \nabla \cdot (\alpha_l \rho_l \boldsymbol{u}_l) = S_m \tag{15}$$

where the mass source term S_m is defined as

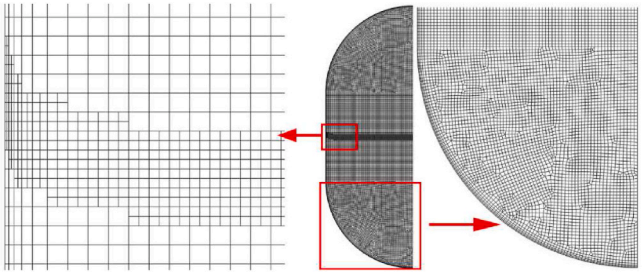

Fig. 2. Mesh distribution inside the axisymmetric scaling capsule tank.

$$S_m = \begin{cases} C\alpha_l \rho_l \dfrac{(T_l - T_{sat})}{T_{sat}}, & T_l > T_{sat}, \text{evaporation} \\ C\alpha_g \rho_g \dfrac{(T_{sat} - T_g)}{T_{sat}}, & T_v < T_{sat}, \text{condensation} \end{cases} \tag{16}$$

according to simplified evaporation-condensation model [40]. C is chosen as 0.1s^{-1} [41] with the assumption that phase change only occurs at the interface. The piecewise-linear method is used for the reconstruction of the interface [42].

Quadrilateral meshes are used for the discretization of calculation domain. Fig. 2 shows the mesh distribution with increasing gradient near the domain boundaries. Adaptive Mesh Refinement (AMR) method [43,44] is adopted to accurately track the interface. In the governing equations, the time derivative is discretized with the first-order upwind scheme and the space derivative is discretized with the second-order upwind scheme. The coupled velocity and pressure are solved using the PISO algorithm.

Validation of the numerical methods is conducted against the K-Site tank self-pressurization experiment carried out in terrestrial condition by Hasan et al. [6]. This experiment used a nearly ellipsoidal liquid hydrogen (LH_2) tank which is constructed of chemical-milled 2219 aluminum and insulated with two blankets of multilayer insulation, each having 17 layers of double aluminized Mylar separated by silk netting. The ratio of the long and short axes is 1.2, with the diameter of the long axis 2.2 m (see Fig. 3a). The volume of the tank is 4.89 m^3. The liquid filling ratio is 85%, with the ambient pressure of 103 kPa. Three cases of heat flux boundary conditions 0.35, 2.0 and 3.5 W/m^2 were applied on the wall of the tank. Then the self-pressurization tests were carried out under steady boil-off initial and isothermal condition.

In the validation of this numerical simulation, the initial temperature was set as the saturation temperature of LH_2 at the pressure 103 kPa, i.e. 20.337 K (data from NIST). The capillary climbing height of LH_2 under the terrestrial condition is about $h \sim \sqrt{\sigma/g(\rho_l - \rho_g)} \simeq 6$ mm, which can be neglected comparing with the characteristic length of the tank ($d \geq 1$ m). Thus, the capillary effect was ignored in the validation of the numerical simulation, i.e., the gas-liquid interface always maintains a flat surface configuration in the process of phase change heat transfer and self-pressurization in this tank. The characteristic velocity of buoyancy convection in the K-Site tank, calculated by $u_z \sim \rho g \beta \Delta T \ell^2/\mu$, is in the order of 10^{-3}~10^{-2} m/s. The corresponding Reynolds number is in the range of 5×10^3~5×10^4. The standard k-ε turbulent model and laminar model are adopted to validate the numerical methods. Detailed mathematical description of the standard k-ε turbulent model can be find in most of the references related to turbulence, thus we will not expand it here.

Fig. 3b shows the temporal evolutions of average gauge pressure $\langle p(\boldsymbol{x},t)\rangle - p_0$ inside the tank based on the laminar and turbulent model for the cases with the wall boundary heat fluxes of 0.35 and 3.5 W/m^2. The average pressure is defined as

$$\langle p(\boldsymbol{x},t)\rangle = \frac{1}{\Omega}\int_{\Omega} p(\boldsymbol{x},t)\, d\Omega \tag{17}$$

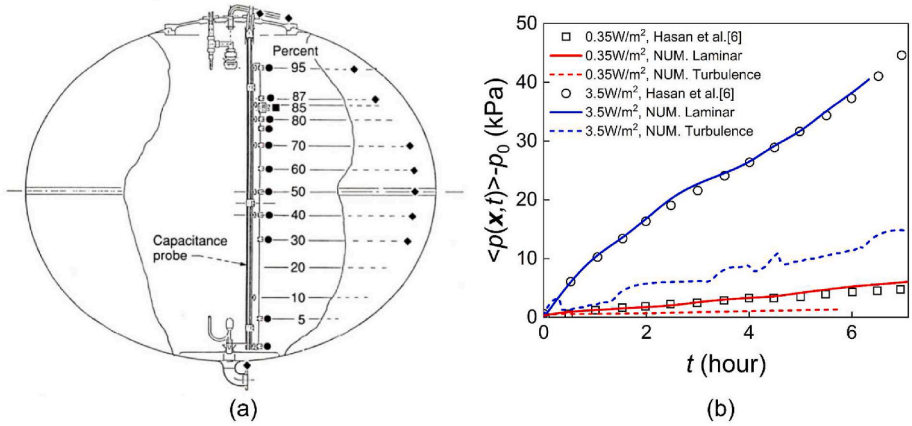

Fig. 3. (A) Apparatus of the K-Site experiment in NASA Glenn Research Center [6], and (b) Benchmark validation of the numerical methods.

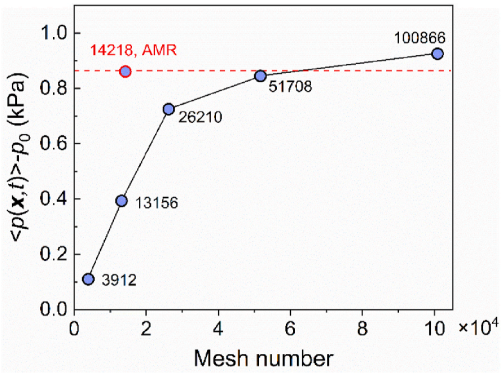

Fig. 4. Grid independence verification.

where Ω is the computational domain, and p_0 is the initial pressure 103 kPa. The results of Laminar model are in good agreement with the K-Site experimental results under steady boil-off initial condition. However, the results based on the turbulent model exhibit significant deviations for both cases. Kassemi et al. also carried out benchmark validation based on the K-Site experiment with the filling ratio of 50% and the heat flux of 3.5 W/m^2 [16,17]. Their study indicates that laminar-conjugated model perform better agreement with experiment results than turbulent model. The relative error of pressure increase in their result in the case of laminar-conjugate model is about 13.7%, which is larger than that (about 2.3%) in our laminar model. Based on this relative small error (about 2.3), it is considered suitable to adopt the laminar model in present numerical study on the scaling propellant storage tank.

Different mesh numbers are adopted to test the grid independence verification. Fig. 4 shows temporal evolutions of the average gauge pressure $\langle p(\boldsymbol{x},t)\rangle - p_0$ inside the ullage for the case with the liquid filling ratio 50% and gravity level $1g_0$. The initial pressure p_0 is 100 kPa at the saturated temperature of 351.12 K. It can be seen that the mesh number of 14,128 with adaptive refinement mesh (AMR) distribution is suitable for future study to balance numerical accuracy and computational efficiency. The time step is 0.00001~0.01s according to the condition that the Currant number remains less than 0.1. The convergence residual is controlled under the relative error of 10^{-5}. The time span of the calculation is 200~300s which is of the order of the characteristic time of thermal conduction in the ullage of the present scaling tank of ethanol.

4. Results and discussion

The heat and mass transfer phenomena in present scaling tank are investigated with various gravity levels, liquid filling ratios and wall boundary heat fluxes. In each case, the equilibrium two-phase distribution in the scaling tank without boundary heat flux is first obtained through the VOF method at the targeted gravity level and then served as the initial state for the succeeding calculations of the heat and mass transfer process. As mentioned above, the capillary effect related to the interface plays an important role in the two-phase flow inside the tank in low-gravity conditions. As an example, Fig. 5 shows the two-phase flow fields inside the tank at 200s with/without consideration of the capillary effect. The liquid filling ratio is 50%, the heat flux is 5 W/m^2 and the gravity level is $10^{-2}g_0$, $10^{-1}g_0$, $1g_0$ respectively. When the capillary effect is ignored (as shown in Fig. 5a–c), the interface remains flat. There is only one major vortex in both the ullage and liquid phases. When the capillary effect is accounted (as shown in Fig. 5d–f), the triple-phase contact line climbs upwards along the tank wall and the interface is convex into the liquid phase. The interface curvature increases with decreasing gravity level. The vortex structure inside the tank becomes complicated, especially in the ullage. The corresponding flow also becomes more intensive. Therefore, the capillary effect related to the interface significantly alters the two-phase flow inside the tank, even in the terrestrial condition. Note that heat and mass transfer are strongly coupled with convection, it is crucial to account the capillary effect related to the interface to accurately predict the thermal and pressure distributions in low-gravity conditions.

4.1. Spatial distributions of thermal and pressure inside the tank

In the present study, the ullage is not fully enveloped by the liquid phase and remains at the top of the tank. The temperature of the two-phase system increases with the continuous heat leakage into the tank. As an example, Fig. 6 shows the temporal evolutions of the isothermals and gauge pressure contours inside the tank with the gravity level $10^{-2}g_0$, boundary heat flux 5 W/m^2 and liquid filling ratio 50%. The gauge pressure is defined as $\Delta p = p\ (\boldsymbol{x},\ t)$ - p_0, and p_0 is 100 kPa at the saturated temperature of 351.12 K. Since the thermal diffusivity of the gas is about 10^2 orders of that of the liquid, the temperature in the ullage rises rapidly compared to the liquid phase. The peak temperature remains at the ullage top, and the heat inside the tank transfers into the bulk of the liquid phase through the interface. Thermal gradient sets up in the ullage region of the tank in both axial and radial directions, while in the liquid phase region the gradient is not obvious. The pressure inside the tank also increases with time. However, the pressure deviation throughout the tank at each moment remains relatively tiny.

Figs. 7–9 show the isothermals and pressure contours inside the tank with various boundary heat fluxes, liquid filling ratios and gravity levels at 200s. The gravity level directly alters interface configuration and

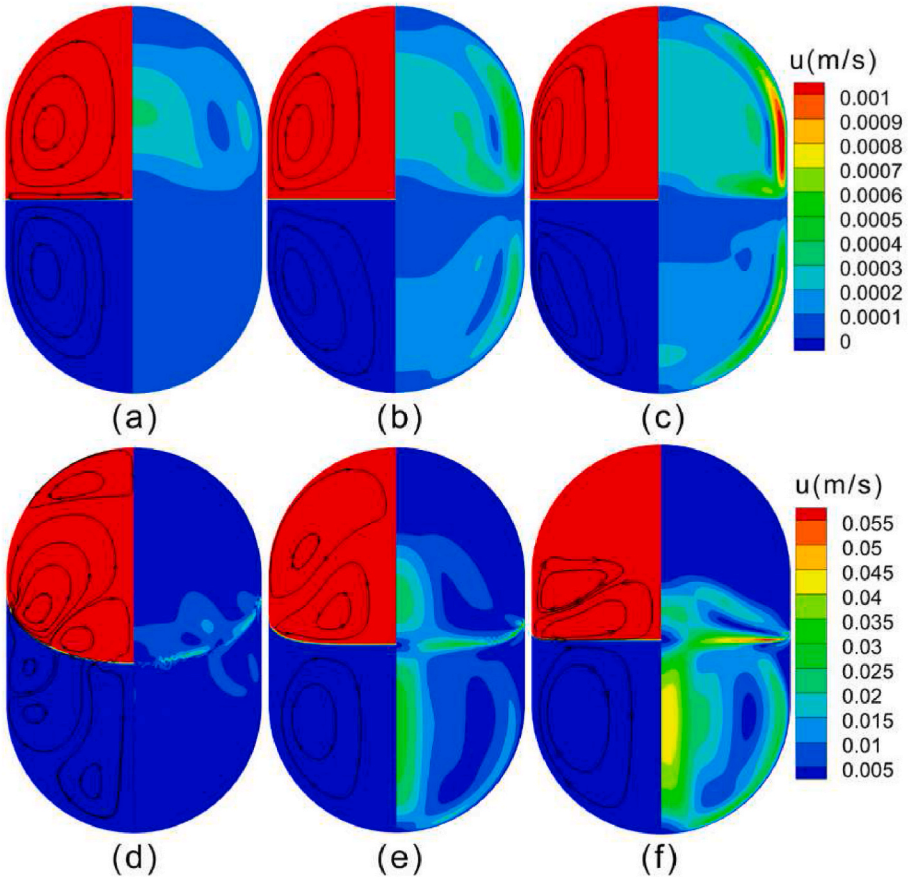

Fig. 5. Streamlines and velocity magnitudes inside the tank at 200s (filling ratio 50%, heat flux 5 W/m^2) without capillary effect (a)$10^{-2}g_0$, (b)$10^{-1}g_0$, (c)$1g_0$, and with capillary effect (d)$10^{-2}g_0$, (e) $10^{-1}g_0$, (f) $1g_0$. Left half of the tanks show two phase distribution, in which the red region stands for vapor and blue region for liquid, and the black lines with arrows stands for streamlines. The right half of the tanks are the contours of velocity magnitude.

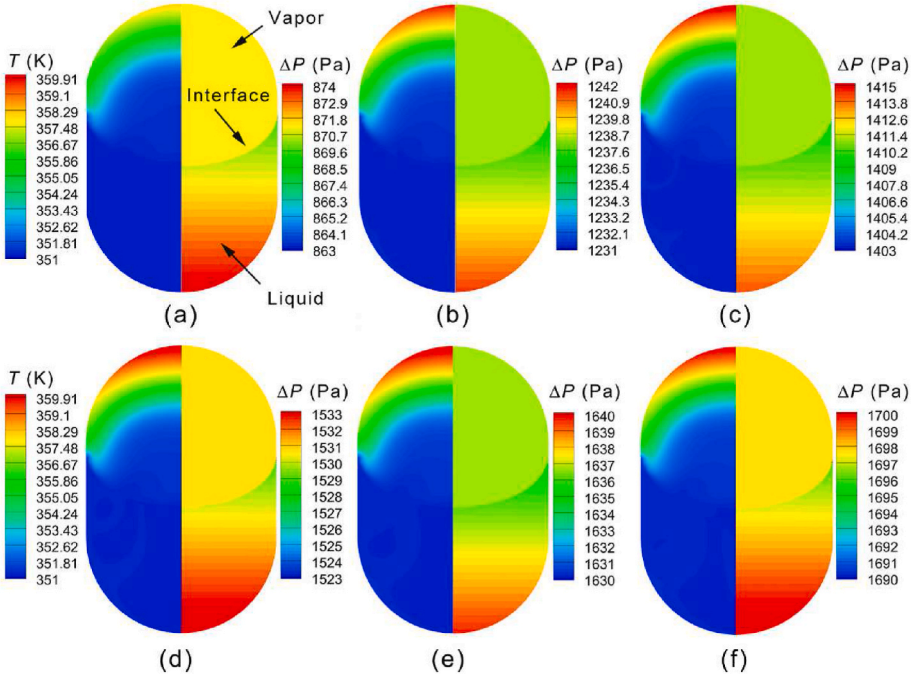

Fig. 6. Temporal evolutions of the isothermals and pressure contours inside the tank with the gravity level $10^{-2}g_0$, boundary heat flux 5 W/m^2 and filling ratio 50%. (a) 50s, (b) 100s, (c) 150s, (d) 200s, (e) 250s, (f) 300s.

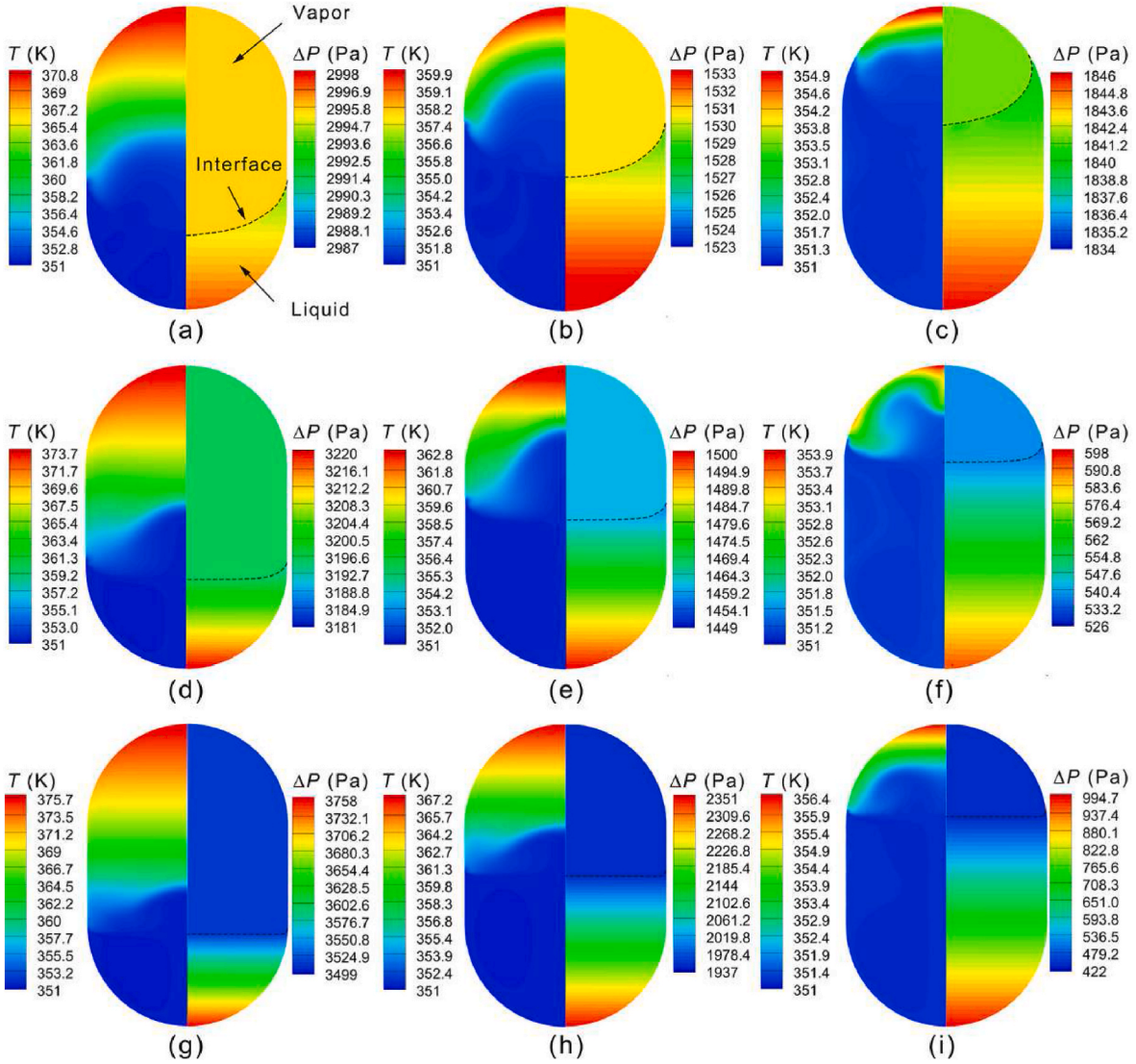

Fig. 7. Isothermals and pressure contours inside the tank at 200s with the boundary heat flux 5 W/m^2, and various gravity levels and filling ratios of (a) $10^{-2}g_0$, 25%, (b) $10^{-2}g_0$, 50%, (c) $10^{-2}g_0$, 75%, (d) $10^{-1}g_0$, 25%, (e) $10^{-1}g_0$, 50%, (f) $10^{-1}g_0$, 75%, (g) $1g_0$, 50%, (h) $1g_0$, 75%, (i) $1g_0$, 75%.

buoyancy convection inside the tank and then affects the thermal and pressure distribution. With the same filling ratio and boundary heat flux, the interface curvature becomes prominent with the decreasing gravity level from $1g_0$ to $10^{-2}g_0$, and the major vortex is prone to break into small ones, as shown in Fig. 5. The decreasing gravity level also decreases the buoyant convection intensity. Therefore, heat transfer inside the tank, especially in the ullage, is weakened. The maximum temperature at the ullage top decreases, as shown in Figs. 7–9 when investigate from the third row up to the first row. The isothermals become more convex towards the ullage top, which results in a steeper temperature gradient in both axial and radial directions. The gauge pressure inside the tank and its maximum difference decrease significantly with the decreasing gravity level. However, the pressure distribution is barely affected by the gravity level change.

With the same boundary heat flux and gravity level, the liquid filling ratio has significant effects on the thermal and pressure distributions inside the tank. The heating area of the ullage and the tank wall increases with the decreasing liquid filling ratio, which results in a significant increase in the maximum temperature inside the tank. For cases with higher liquid filling ratios, the cold region accounts for a larger proportion of the ullage, and the isotherms are denser in the region near the tank wall. It is because for high liquid filling ratio cases, the space of the ullage is smaller, thus most of the space is in the influence domain of the convection vortex. The temperature in the center of the vortex is lower, and the temperature field is redistributed by thermal convection. Therefore, due to the combined effect of heat conduction and convection, flows with a higher temperature are concentrated in the near-wall region of the ullage for cases with higher liquid filling rations. The overall pressure increase inside the tank is significant with the decreasing liquid filling ratio. However, the pressure distribution inside the tank nearly remains unchanged with various liquid filling ratios.

With the same liquid filling ratio and gravity level, the overall temperature and pressure rises are significant with the increasing boundary heat flux. The thermal distribution in the ullage becomes less convex towards the ullage top, and the temperature gradient becomes axial only, as compared between Figs. 7–9. The pressure distribution inside the tank nearly remains unchanged with various boundary heat fluxes.

4.2. *Temporal evolutions of thermal and pressure inside the tank*

Note that it is important to predict the temporal evolutions of the thermal and pressure distributions inside the tank for practical engineering applications. As an example, Fig. 10 shows temporal evolutions of the temperature and gauge pressure along the symmetric axis of the

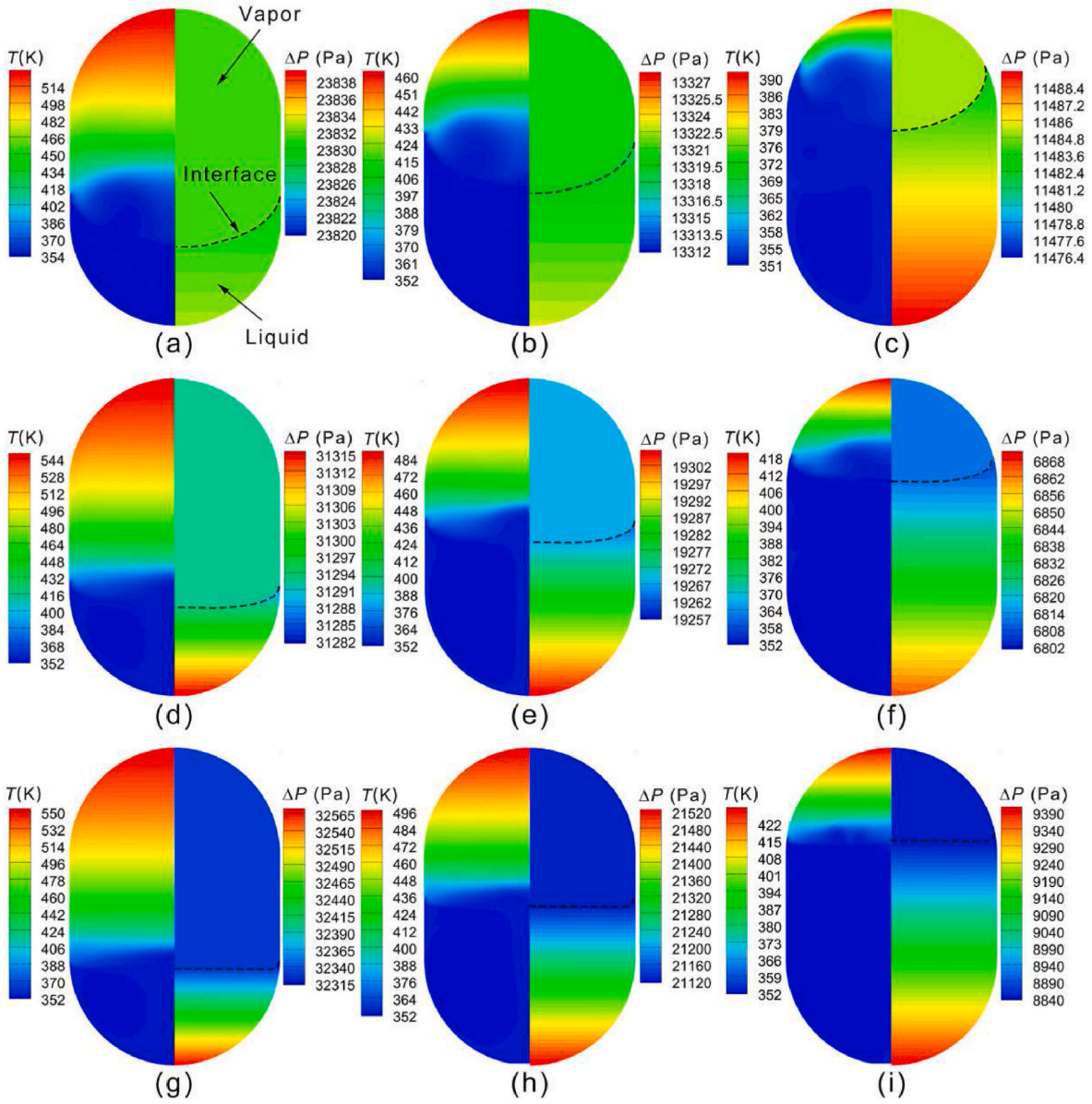

Fig. 8. Isothermals and pressure contours inside the tank at 200s with the boundary heat flux 50 W/m^2 and various gravity levels and filling ratios of (a) $10^{-2}g_0$, 25%, (b) $10^{-2}g_0$, 50%, (c) $10^{-2}g_0$, 75%, (d) $10^{-1}g_0$, 25%, (e) $10^{-1}g_0$, 50%, (f) $10^{-1}g_0$, 75%, (g) $1g_0$, 50%, (h) $1g_0$, 75%, (i) $1g_0$, 75%.

tank with gravity level $10^{-2}g_0$, boundary heat flux 5 W/m^2 and liquid filling ratio of 50%. It can be seen that a prominent thermal gradient emerges along the axis (this also can be seen in Fig. 7b). Both the temperature and pressure increase with time, and the increasing extent in the same time interval decreases. However, the pressure along the axis approximately remains constant at each moment.

Fig. 11 shows the temporal evolutions of average temperature $\langle T(\boldsymbol{x},t)\rangle$ inside the tank dependent on various boundary heat fluxes, liquid filling ratios and gravity levels. $\langle T(\boldsymbol{x},t)\rangle$ is defined as

$$\langle T(\boldsymbol{x},t)\rangle = \frac{1}{\Omega}\int_{\Omega} T(\boldsymbol{x},t)\, d\Omega \tag{18}$$

Generally, the average temperature initially increases rapidly with time, and then the increasing rate decreases. The average temperature and the boundary heat flux are positively correlated, e.g., for the case with the liquid filling ratio 25% and gravity level $10^{-2}g_0$, the average temperature at 300s is 357.44 K, 413.63 K and 459.69 K with the boundary heat flux 5, 50 and 100 W/m^2, respectively. The relative increase extents with respect to the initial temperature of 351.12 K are 1.8%, 17.8% and 30.9%. With the same liquid filling ratio and boundary heat flux, the increasing rate of the average temperature in the regime from $10^{-2}g_0$ to $10^{-1}g_0$ is much faster than it in the regime from $10^{-1}g_0$ to $1g_0$. On the other hand, with the same boundary heat flux and gravity level, the average temperature at 300 s significantly increases with decreasing liquid filling ratio. As mentioned above, the overall pressure inside the tank increases with time, however, the pressure approximately remains constant throughout the tank.

Fig. 12 shows temporal evolutions of the average gauge pressure $\langle p(\boldsymbol{x},t)\rangle - p_0$ inside the tank with various boundary heat fluxes, liquid filling ratios and gravity levels. The profiles exhibit similar trends as those of the average temperature. The average pressure significantly increases with increasing boundary heat flux and decreasing liquid filling ratio, e.g., the average pressure rise at 300 s is about 60 kPa for the liquid filling ratio of 25% and 15 kPa for the liquid filling ratio of 75%, respectively. On the other hand, the gravity level has less influence on the average pressure.

Figs. 11–12 also illustrate the influence of the capillary effect at the interface on the temporal evolutions of the average temperature and

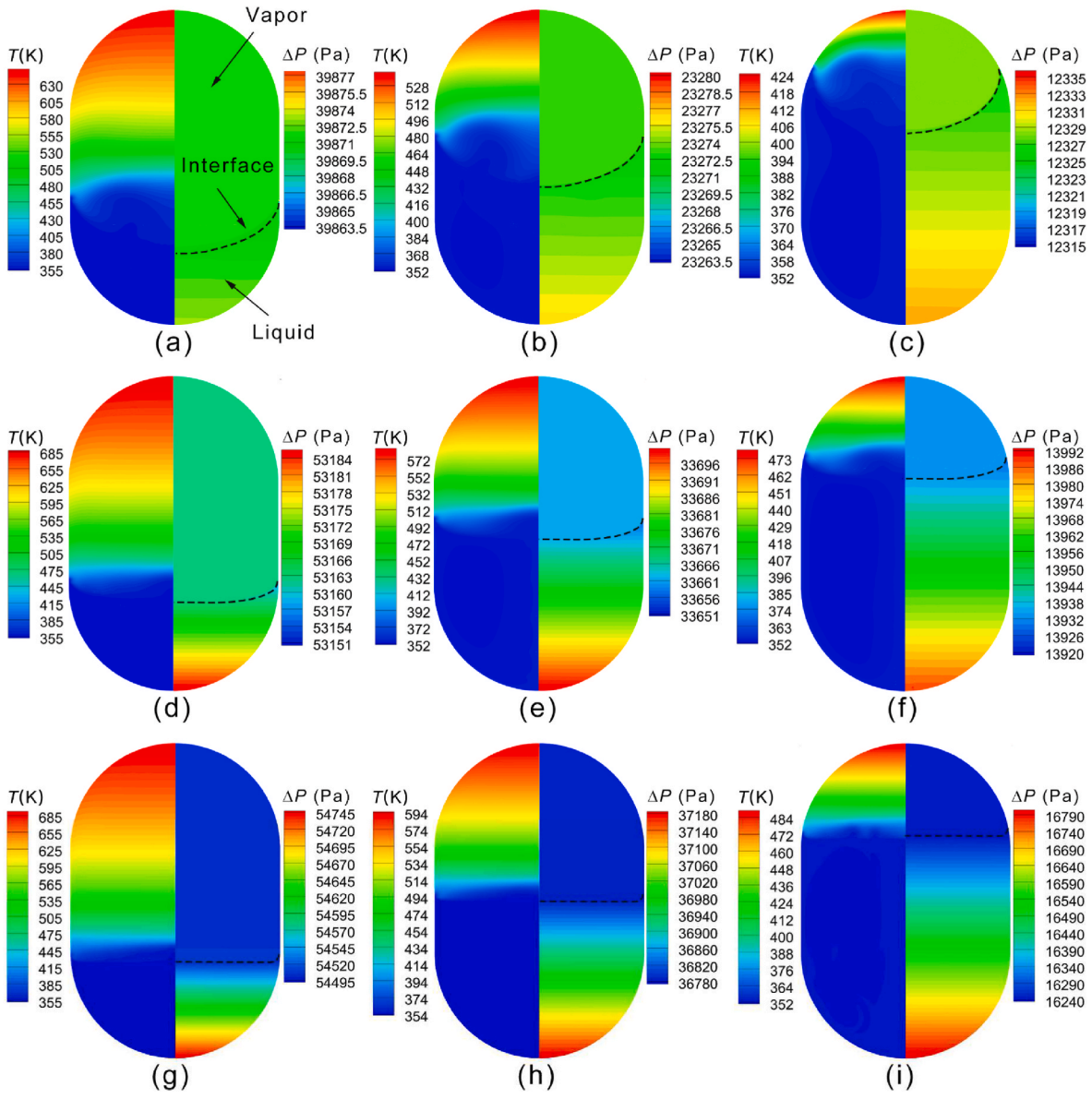

Fig. 9. Isothermals and pressure contours inside the tank at 200s with the boundary heat flux 100 W/m^2 and various gravity levels and filling ratios of (a) $10^{-2}g_0$, 25%, (b) $10^{-2}g_0$, 50%, (c) $10^{-2}g_0$, 75%, (d) $10^{-1}g_0$, 25%, (e) $10^{-1}g_0$, 50%, (f) $10^{-1}g_0$, 75%, (g) $1g_0$, 50%, (h) $1g_0$, 75%, (i) $1g_0$, 75%.

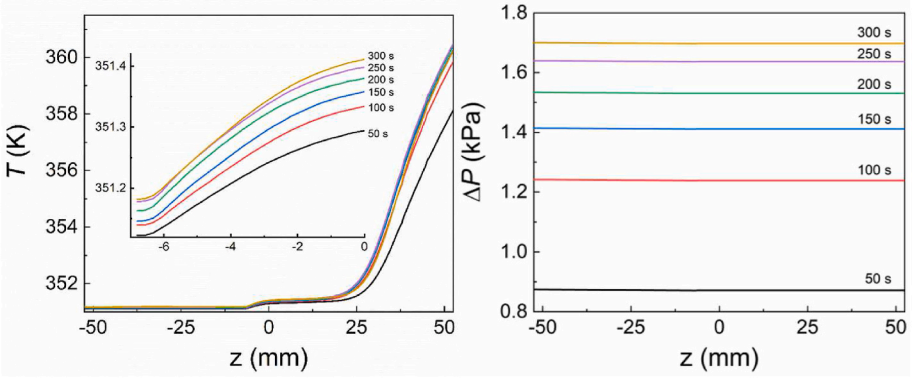

Fig. 10. Temporal evolutions of the temperature and pressure along the symmetric axis of the tank with gravity level $10^{-2}g_0$, boundary heat flux 5 W/m^2 heat flux and filling ratio 50%.

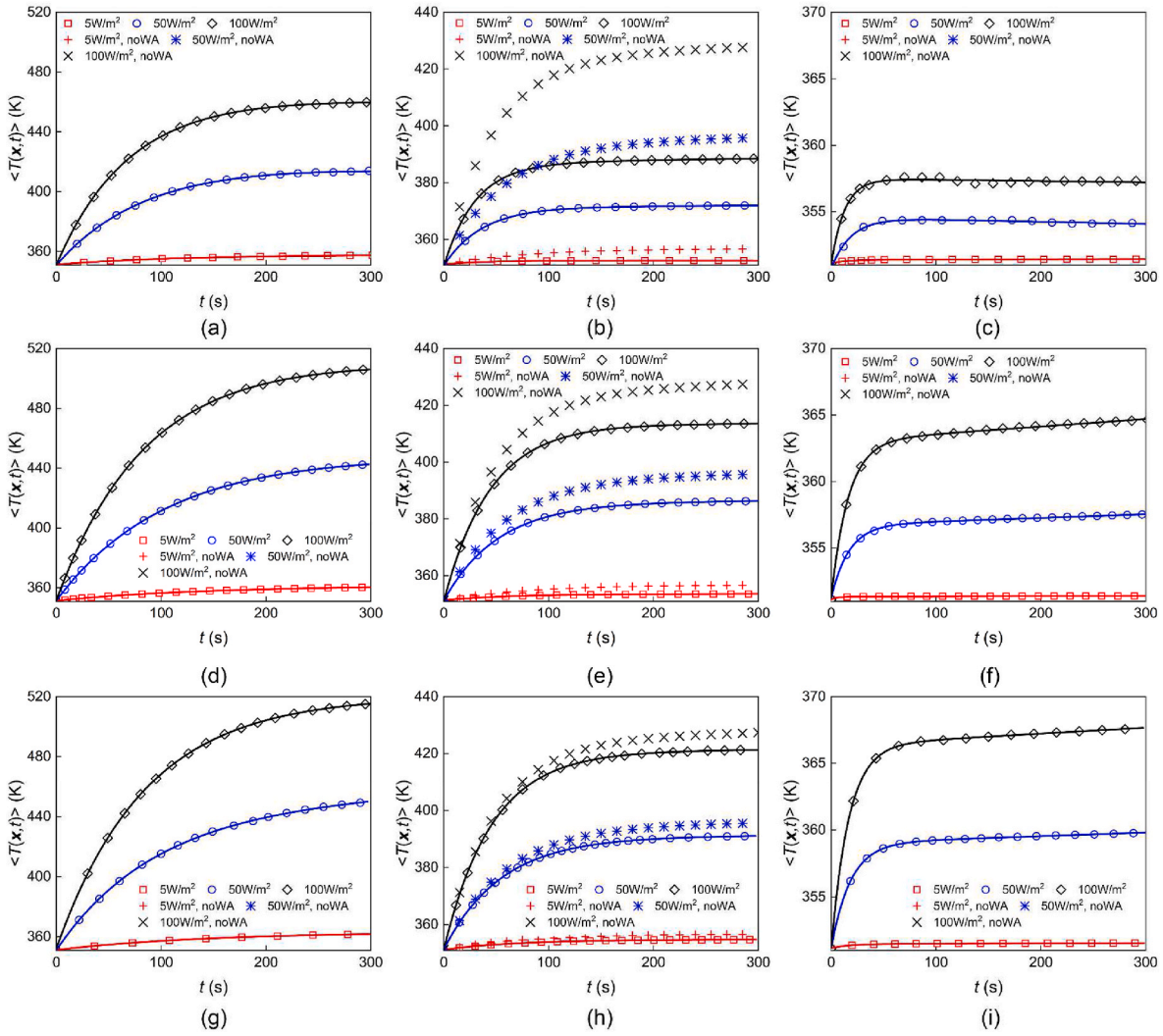

Fig. 11. Temporal evolutions of the average temperature inside the tank dependent on various boundary heat fluxes, liquid filling ratios and gravity levels. The case with noWA means the capillary effect is ignored. The gravity levels and filling ratios are (a) $10^{-2}g_0$, 25%, (b) $10^{-2}g_0$, 50%, (c) $10^{-2}g_0$, 75%, (d) $10^{-1}g_0$, 25%, (e) $10^{-1}g_0$, 50%, (f) $10^{-1}g_0$, 75%, (g) $1g_0$, 25%, (h) $1g_0$, 50%, (i) $1g_0$, 75%.

pressure. When the capillary effect at the interface is ignored, the interface in the tank remains flat and the gas/liquid phase distribution is independent of gravity level, as shown in Fig. 5a–c. The temporal evolutions of the predicted average temperature and pressure are overestimated compared to the case accounting for the capillary effect, and the deviation becomes significant with decreasing gravity level. For example, it is about 105% for relative temperature increasing $\langle T(\boldsymbol{x},t)\rangle - T_0$ and 86% for gauge pressure $\langle p(\boldsymbol{x},t)\rangle - p_0$ at 300s for the cases with the gravity level $10^{-2}g_0$, boundary heat flux 100 W/m^2 and the liquid filling ratio 50%, respectively. Moreover, the temporal evolutions of the average temperature and pressure predicted ignoring the capillary effect are approximately independent of the gravity level, while those are strongly dependent on the gravity level for the cases accounting for the capillary effect. Therefore, it is crucial to account for the capillary effect to accurately predict the temporal evolutions of the thermal and pressure distributions inside the tank in low-gravity conditions.

4.3. Mass transfer process at the interface inside the tank

In the present study, the phase change process at the interface is strongly coupled with the heat transfer inside the tank. During the phase transition, the release/absorption of the latent heat alters the local temperature field of the interface region and then modifies the overall thermal and pressure distributions inside the tank. It in turn influences the phase change process.

Fig. 13 shows the temporal evolutions of mass flow rate at the interface dependent on various boundary heat fluxes, liquid filling ratios and gravity levels. The mass flow rate is defined as the integral of the mass source S_m over the computational domain Ω. A negative value indicates the evaporation process while a positive value indicates the condensation process. Generally, the mass transfer at the interface experiences several stages. In the initial stage (stage 1 in Fig. 13), the local temperature in the region of the triple-phase contact line rises due to the heat transfer through the tank wall. When it exceeds the saturation temperature at the initial pressure inside the tank, the evaporation process occurs. The continuous boundary heat transfer enhances the evaporation process. On the other hand, the evaporation process is weakened through the following mechanisms. One is that the latent heat absorbed in the evaporation process decreases the local temperature at the interface. The other one is that due to the heat transfer in the bulk of the tank, the ullage is heated which not only increases the ullage pressure and then the corresponding saturation temperature, but also induces the condensation process in the central region of the interface. With the competition of these mechanisms, the magnitude of the mass flow rate initially increases rapidly, and then gradually decreases after a local maximum. The profile of the mass flow rate exhibits a concave

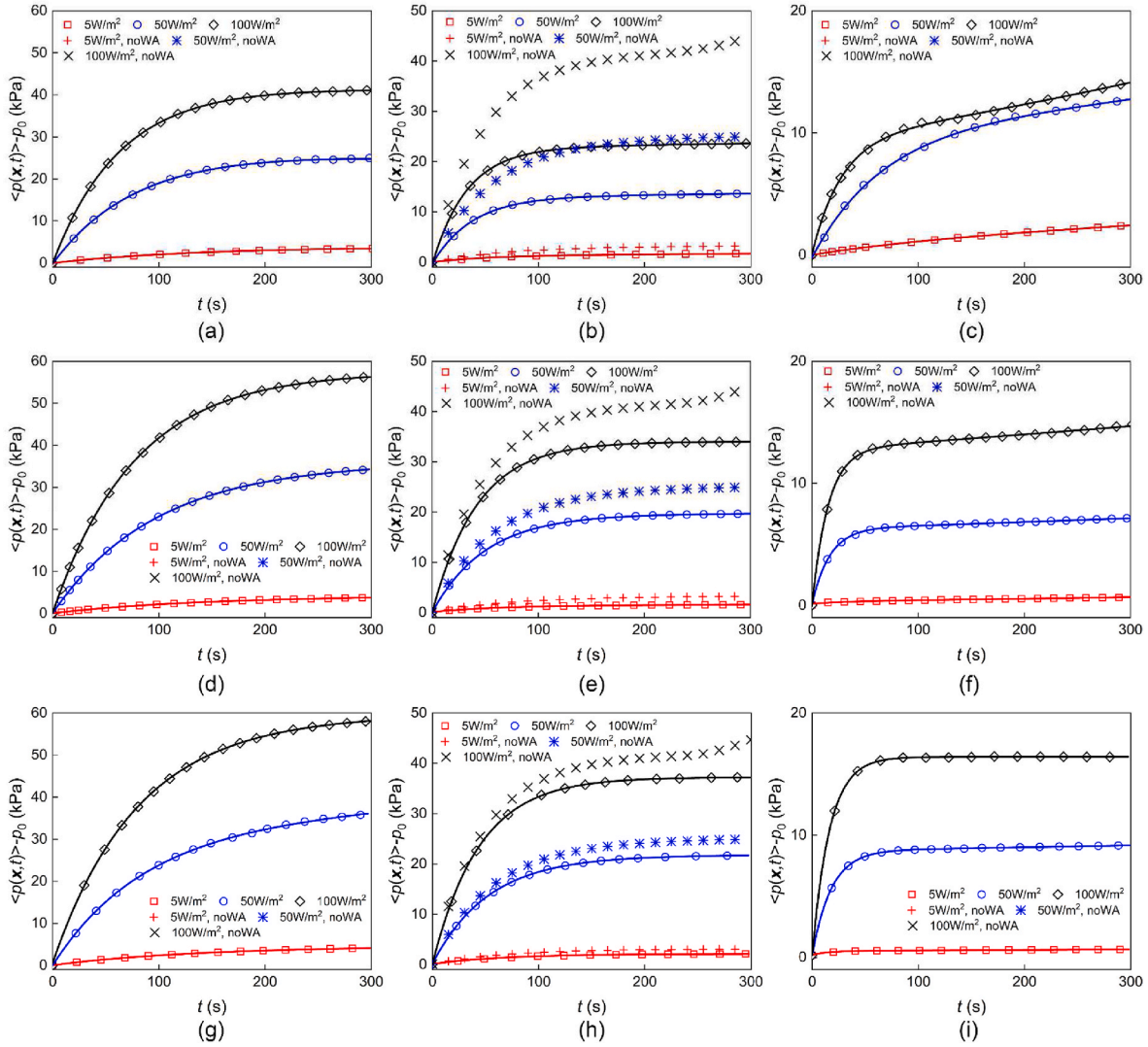

Fig. 12. Temporal evolutions of the average gauge pressure inside the tank dependent on various boundary heat fluxes, liquid filling ratios and gravity levels. The case with noWA means the capillary effect is ignored. The gravity levels and filling ratios are (a) $10^{-2}g_0$, 25%, (b) $10^{-2}g_0$, 50%, (c) $10^{-2}g_0$, 75%, (d) $10^{-1}g_0$, 25%, (e) $10^{-1}g_0$, 50%, (f) $10^{-1}g_0$, 75%, (g) $1g_0$, 25%, (h) $1g_0$, 50%, (i) $1g_0$, 75%.

shape with time. Both the increase and decrease trends of the mass flow rate become steeper with the increasing boundary heat flux. In the stable stage (stage 2 in Fig. 13), the total effect of evaporation maintains at the interface with greatly reduced intensity for the cases with the gravity level $10^{-2}g_0$. With increasing gravity level and boundary heat flux, the intensified heat transfer inside the tank significantly increases the ullage pressure and the corresponding saturation temperature. The enhanced condensation process results in a positive mass flow rate contrary to the case with the boundary heat flux 5 W/m^2. However, the time interval of the stage 2 decreases with the increasing liquid filling ratio, and the total effect of evaporation dominates again in the following stage (stage 3 in Fig. 13), especially for the cases with a high liquid filling ratio of 75% and large boundary heat flux. The trend is consistent with temporal evolutions of the average temperature and the pressure distribution shown in Figs. 11–12.

Fig. 14 shows the total mass flow rate at the interface dependent on various boundary heat fluxes, liquid filling ratios and gravity levels when the capillary effect is ignored. For the cases with the wall boundary heat fluxes 5 W/m^2 and 50 W/m^2, the mass flow rate is nearly zero during the entire time span. While for the rest cases, the total effect of evaporation occurs at 200s and becomes intense with time increase. The phenomena are significantly different from those cases accounting for the capillary effect at the interface. The reason is that the evaporation process with the curved interface is enhanced due to the larger interaction surface of the thin liquid film in the region of the triple-phase contact line compared to the restricted one for the case with the planar interface (see Fig. 15). Therefore, the capillary effect at the interface greatly influences the mass transfer process, as well as the thermal and pressure distribution discussed in the previous section.

4.4. Heat transfer process inside the tank

The heat transfer inside the tank is described by the energy equation (see Eq. (4)). It can be seen that the unsteady term in Eq. (4) is approximately described by $O(\Delta T/t)$, the advection term by $O(u\Delta T/R)$ and the diffusion term by $O(\lambda\Delta T/\delta^2)$, where the thickness of thermal layer $\delta \ll R$, ΔT denotes the temperature difference between the heated tank wall and the axis of the tank. Since the unsteady term is large compared to the advection term in a small time scale, the thermal layer yields

$$\delta \sim \lambda^{1/2} t^{1/2} \tag{19}$$

and the temperature deference ΔT at the initial time period can be given by

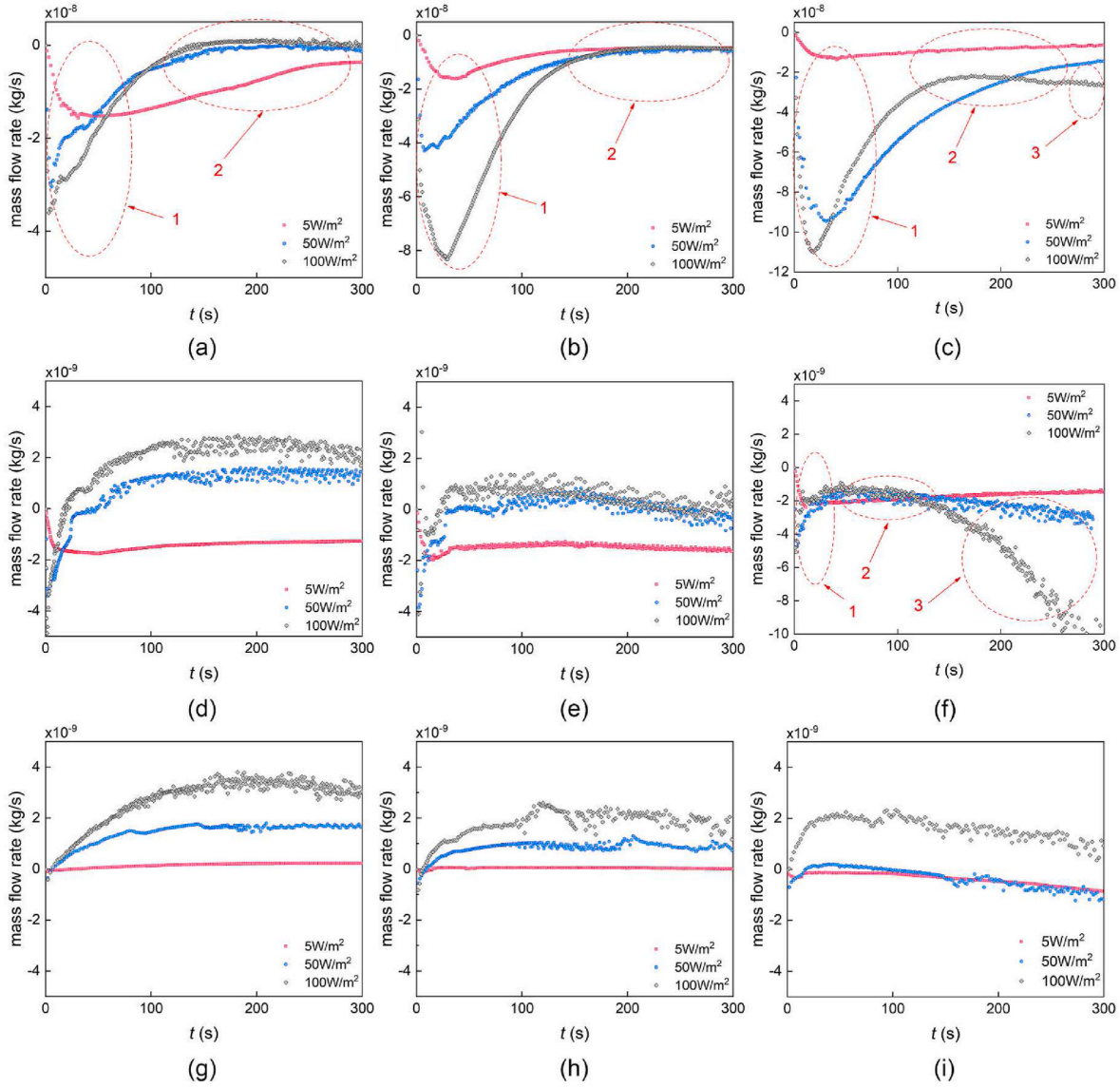

Fig. 13. Temporal evolutions of the mass flow rate at the interface dependent on different boundary heat fluxes of 5, 50 and 100 W/m^2, with the liquid filling ratios and gravity levels of (a) $10^{-2}g_0$, 25%, (b) $10^{-2}g_0$, 50%, (c) $10^{-2}g_0$, 75%, (d) $10^{-1}g_0$, 25%, (e) $10^{-1}g_0$, 50%, (f) $10^{-1}g_0$, 75%, (g) $1g_0$, 25%, (h) $1g_0$, 50%, (i) $1g_0$, 75%.

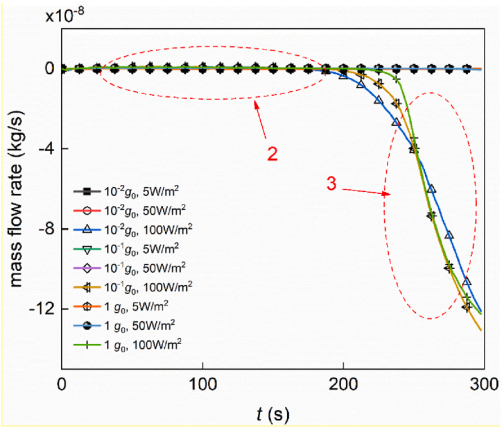

Fig. 14. Temporal evolutions of the mass flow rate at the interface dependent on various boundary heat fluxes, liquid filling ratios and gravity levels when the capillary effect is ignored.

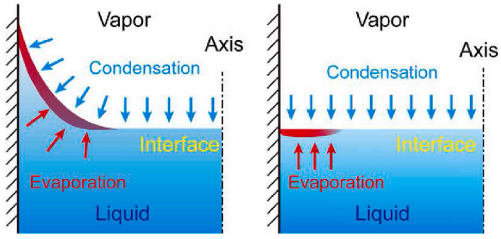

Fig. 15. Schematic of the evaporation and condensation process occurs at the interface w/o considering the capillary effect.

$$\Delta T \sim q''\delta/k \tag{20}$$

This means the heat transfer is dominated by thermal conduction regime.

The characteristic time scale in terms of thermal conduction (t_1), thermocapillary (t_2) and buoyancy convection (t_3) can be derived by dimensional analysis, with the result of

Table 2
Characteristic time and velocity scale of thermal conduction, thermocapillary and buoyancy convection, and the dimensionless numbers for ethanol at 360 K in the condition of 10^{-2} g_0, $\Delta T = 1$ K.

Parameters	C_2H_5OH(l)	C_2H_5OH(g)
t_1 (s)	17804.1	214.086
t_2 (s)	0.1639	–
t_3 (s)	0.1153	–
u_t (m/s)	1.966E-6	1.635E-4
u_c (m/s)	0.2136	–
u_z (m/s)	0.3035	–
Pr	7.78	–
Ma	1.086 E+05	–
Ra	1.544 E+05	–

$$t_1 \sim \ell^2/\lambda \tag{21}$$

$$t_2 \sim \frac{\mu \ell}{\sigma_T \Delta T} \tag{22}$$

$$t_3 \sim \frac{\nu}{g\ell\beta\Delta T} \tag{23}$$

Similarly, the characteristic velocity corresponding to thermal conduction (u_t) is

$$u_t \sim \lambda/\ell \tag{24}$$

to thermocapillary (u_c) and buoyancy convection (u_z) is given in Eqs. (13) and (14). Then, it is found that

$$\frac{t_1}{t_2} = \frac{u_c}{u_t} \sim Ma \tag{25}$$

$$\frac{t_1}{t_3} = \frac{u_z}{u_t} \sim Ra \tag{26}$$

$$\frac{t_2}{t_3} = \frac{u_z}{u_c} \sim \frac{\rho g \beta \ell^2}{\sigma_T} \sim \frac{\rho g \beta \Delta T \ell^2}{\sigma} = \frac{Ra}{Ma} \tag{27}$$

Without loss of generality, we chose the property values of Ethanol at 360 K in the condition of in the condition of $10^{-2}g_0$, $\Delta T = 1$ K, to calculate the corresponding characteristic values of time, velocity and dimensionless number, as shown in Table 2. It is found that the characteristic time scale of thermal conduction t_1 for the liquid phase (i.e. the time of heat transfer from the wall to the axis of the tank) is within 5 h for the scaling tank. In comparison, the characteristic time scale of thermal conduction for the vapor phase is only 214 s, which is much smaller than that of the liquid phase. Under the condition of $10^{-2}g_0$ and $\Delta T = 1$ K, $t_2 \sim t_3 \ll t_1$, namely the flow field is dominated by natural convection. Additionally, Equation (27) indicates that the competition of convection between the thermocapillary and buoyancy effects is proportional to the gravity level *g*, even though that the thermocapillary convection only acts on the two-phase interface, while the buoyancy convection acts on the bulk liquid phase.

The Nusselt number (*Nu*) plays an important role in the heat transfer process near the wall of the propellant tank. Generally, $Nu = f(\boldsymbol{x}, Re, Pr)$ for given physical models, reflecting the relative strength of thermal

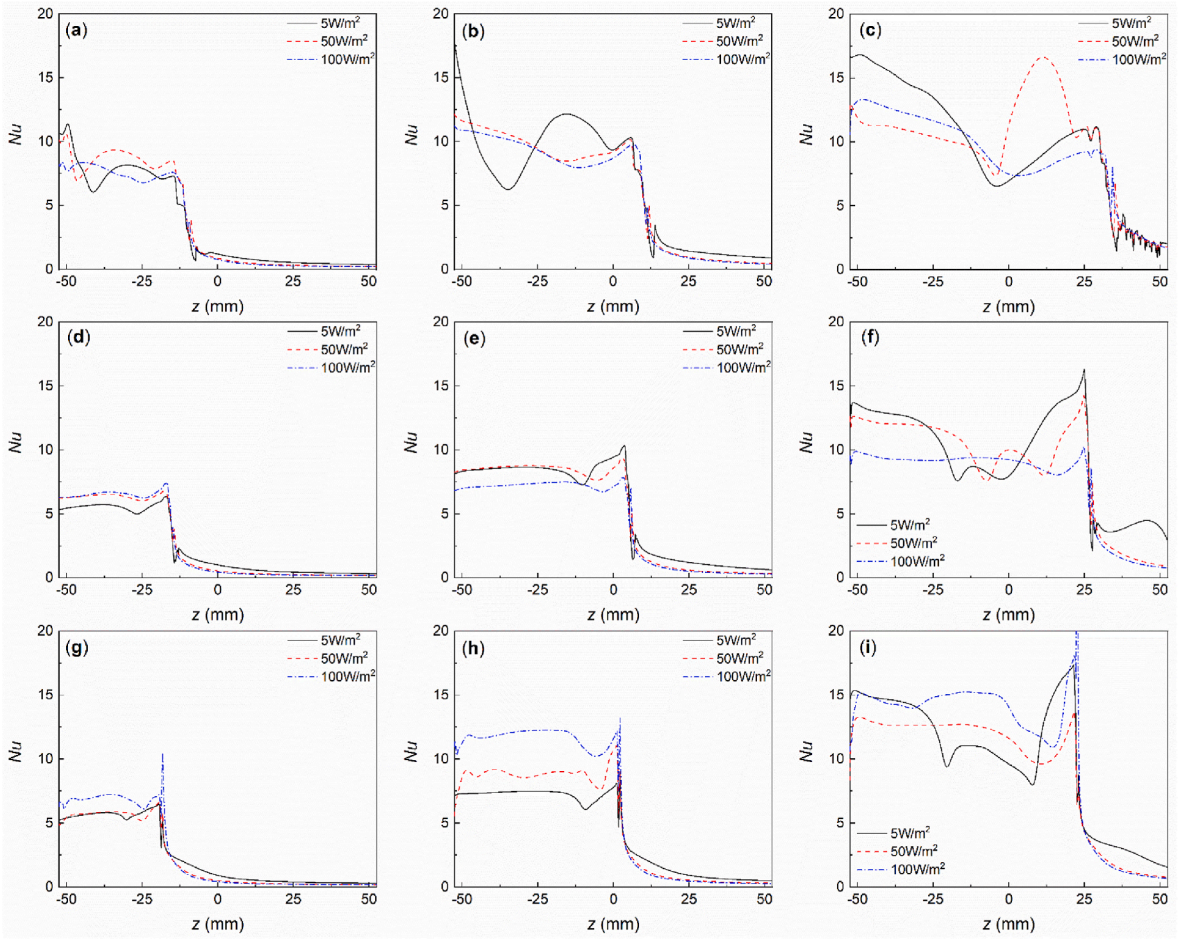

Fig. 16. Nusselt number (*Nu*) distribution on the wall of tank in *z* direction at 200s for different boundary heat fluxes of 5, 50 and 100 W/m^2, with the liquid filling ratios and gravity levels of (a) $10^{-2}g_0$, 25%, (b) $10^{-2}g_0$, 50%, (c) $10^{-2}g_0$, 75%, (d) $10^{-1}g_0$, 25%, (e) $10^{-1}g_0$, 50%, (f) $10^{-1}g_0$, 75%, (g) $1g_0$, 25%, (h) $1g_0$, 50%, (i) $1g_0$, 75%.

convection and conduction. In present study, *Nu* is given by

$$Nu = \frac{h\ell}{k} \tag{28}$$

where the heat transfer coefficient h can be expressed as

$$h = \frac{q''}{T_w - T_0} \tag{29}$$

Here, temperature T_w on the wall of tank changes with time under constant heat flux q'', and the initial temperature $T_0 = 351.12$ K.

Fig. 16 shows the Nusselt number distribution on the wall of tank in z direction at 200s for different boundary heat fluxes of 5, 50 and 100 W/m^2. It can be seen that the $Nu \sim 10^1$ at the liquid region and $Nu \sim 1$ at the vapor region for all of the cases, which indicates that the heat transfer in liquid phase is dominated by convection and in vapor phase both by convection and conduction. Specifically, the buoyancy convection promotes the heat transfer process in liquid phase, while the convection in the vapor phase mainly owes to the Marangoni effect on the interface. The *Nu* in liquid phase remains nearly constant and same for different boundary heat fluxes (5, 50 and 100 W/m^2) and gravity levels (column panels in Fig. 16). The fluctuations of *Nu* from the bottom to the interface results from the vortices flow (see Fig. 5d) in liquid phase, especially for the low gravity cases, as shown in Fig. 16a–c. However, the *Nu* in vapor phase for 5 W/m^2 is larger than that for 50 and 100 W/m^2. This is due to the strengthen of thermal conduction for higher heat flux. It can be found from Fig. 16 that the *Nu* is larger for higher liquid filling ratios, especially in the liquid phase region. In addition, there are slight risings of *Nu* near the triple-phase region due to the strong thermocapillary convection.

5. Conclusion

The heat and mass transfer process of the gas/liquid two-phase flow with the capillary effect accounted at the interface in a storage tank and its dependencies on the gravity level, liquid filling ratio, and boundary heat flux are investigated. Here are the conclusions.

According to the spatial-temporal evolutions of the thermal and pressure fields, the temperature and pressure along the symmetric axis first increase rapidly and then the increasing rate slows down as time goes by, and temporal evolutions of the average temperature and pressure have similar trends. The increase in temperature in the ullage is more significant and the gauge pressure is almost the same along the symmetric axis at each moment.

The increasing gravity level, boundary heat flux and the decreasing liquid filling ratio intensify the heat transfer in the tank, which makes the thermal and pressure distributions in the tank more uniform and causes the overall temperature and pressure to increase. This phenomenon mainly results from the larger area of heating in these conditions. Therefore, the low-liquid filling ratio tank should be focused on in industrial applications.

Both the thermal and pressure distributions and the mass transfer rate are significantly affected when the capillary effect at the interface is considered. Moreover, the influence of the gravity level is essentially due to the various interface configurations caused by capillary effect. Therefore, it is crucial to account for the capillary effect at the interface to accurately predict the thermal and pressure distributions in a low-gravity environment.

Note that the actual application environment is much more complex than the simplified models of numerical simulation for the scaled propellant storage tank, and the results will be different for detailed parameters. Especially for large scale storage tank, the heat and mass transfer process require larger time scale to reach the thermal and pressure state obtained in this research. And the accurate acquisition of the flow field in a large scale tank is time consuming. However, the methodology (especially the consideration of capillary effect) used in this study, the analysis method and the patterns obtained from this work still have certain industry guidance significance for investigation of the spatial-temporal evolutions of thermal and pressure distributions in a tank.

Declaration of competing interest

The authors declare that they have no known competing financial interests or personal relationships that could have appeared to influence the work reported in this paper.

Data availability

Data will be made available on request.

Acknowledgements

This research is supported by the National Natural Science Foundation of China (No. 12172363) and the China Postdoctoral Science Foundation (No. 2022M711428).

References

[1] A.F. Schmidt, J.R. Purcell, W.A. Wilson, R.V. Smith, An experimental study concerning the pressurization and stratification of liquid hydrogen, in: K. D. Timmerhaus (Ed.), Advances in Cryogenic Engineering, Springer US, Boston, MA, 1960, pp. 487–497.
[2] D.O. Barnett, L.S. Mcreynolds, T.W. Winstead, An Investigation of Liquid-Hydrogen Stratification in a Large Cylindrical Tank of the Saturn Configuration, 1965.
[3] J.C. Aydelott, C.M. Spuckler, Effect of Size on Normal-Gravity Self-Pressurization of Spherical Liquid Hydrogen Tankage, 1969.
[4] J.C. Aydelott, Normal Gravity Self-Pressurization of 9-inch-/23 cm/diameter Spherical Liquid Hydrogen Tankage, 1967.
[5] J.C. Aydelott, Effect of Gravity on Self-Pressurization of Spherical Liquid-Hydrogen Tankage, 1967.
[6] M. Hasan, C.S. Lin, N. Vandresar, Self-pressurization of a Flightweight Liquid Hydrogen Storage Tank Subjected to Low Heat Flux, ASME/AIChE National Heat Transfer Conference, 1991, 1991.
[7] C. Lin, M. Hasan, Self-pressurization of a Spherical Liquid Hydrogen Storage Tank in Amicrogravity Environment, 30th Aerospace Sciences Meeting and Exhibit, 1992, p. 363.
[8] J. Hochstein, H.C. Ji, J. Aydelott, Effect of subcooling on the on-orbit pressurization rate of cryogenic propellant tankage, in: 4th Thermophysics and Heat Transfer Conference, 1986, p. 1253.
[9] J.I. Hochstein, H.C. Jit, J.C. Aydelott, Prediction of self-pressurization rate of cryogenic propellant tankage, J. Propul. Power 6 (1990) 11–17.
[10] G. Grayson, A. Lopez, F. Chandler, L. Hastings, A. Hedayat, J. Brethour, CFD modeling of helium pressurant effects on cryogenic tank pressure rise rates in normal gravity, in: 43rd AIAA/ASME/SAE/ASEE Joint Propulsion Conference & Exhibit, 2007, p. 5524.
[11] S. Barsi, M. Kassemi, Numerical and experimental comparisons of the self-pressurization behavior of an LH2 tank in normal gravity, Cryogenics 48 (2008) 122–129.
[12] S. Barsi, M. Kassemi, Investigation of tank pressurization and pressure control—Part I: experimental study, J. Therm. Sci. Eng. Appl. 5 (2013), 041005.
[13] S. Barsi, M. Kassemi, Investigation of tank pressurization and pressure control—Part II: numerical modeling, J. Therm. Sci. Eng. Appl. 5 (2013), 041006.
[14] L. Chen, G. Liang, Simulation research of vaporization and pressure variation in a cryogenic propellant tank at the launch site, Microgravity Sci. Technol. 25 (2013) 203–211.
[15] O.V. Kartuzova, M. Kassemi, J.H. Agui, J.P. Moder, A CFD model for the multipurpose hydrogen test bed (MHTB) ground-based self-pressurization and pressure control experiments, in: 11th AIAA/ASME Joint Thermophysics and Heat Transfer Conference, 2014, p. 3361.
[16] M. Kassemi, O. Kartuzova, Effect of interfacial turbulence and accommodation coefficient on CFD predictions of pressurization and pressure control in cryogenic storage tank, Cryogenics 74 (2016) 138–153.
[17] M. Kassemi, O. Kartuzova, S. Hylton, Validation of two-phase CFD models for propellant tank self-pressurization: crossing fluid types, scales, and gravity levels, Cryogenics 89 (2018) 1–15.
[18] Z. Liu, Y. Li, G. Zhou, Study on thermal stratification in liquid hydrogen tank under different gravity levels, Int. J. Hydrogen Energy 43 (2018) 9369–9378.
[19] Z. Liu, G. Zhou, Y. Li, P. Gao, Thermal performance of liquid hydrogen tank in reduced gravity, Adv. Space Res. 62 (2018) 957–966.
[20] Z. Liu, Y. Li, G. Zhou, Insulation performance of foam during the terrestrial and ascent period, Appl. Therm. Eng. 145 (2018) 364–374.
[21] L. Wang, T. Yan, J. Wang, S. Ye, Y. Li, R. Zhuan, B. Wang, CFD investigation on thermodynamic characteristics in liquid hydrogen tank during successive varied-gravity conditions, Cryogenics 103 (2019), 102973.

[22] F. Xie, Y. Li, K. Zhu, Y. Ma, J. Wang, Cooling behaviors of liquid hydrogen by helium gas injection, Heat Mass Tran. 55 (2019) 2373–2390.
[23] Z. Liu, J. Cui, J. Yan, G. Zhou, Y. Li, Effect of initial parameter on thermodynamic performance in a liquid oxygen tank with pressurized helium gas, Science and Technology for the Built Environment 26 (2020) 426–436.
[24] G. Wang, J. Li, Y. Zhao, G. Hong, Analysis of a new self-pressurization model for cryogenic fluid tank, in: IOP Conference Series: Materials Science and Engineering, IOP Publishing, 2019, 012064.
[25] S. Vishnu, B.T. Kuzhiveli, Mathematical modeling of thermal stratification in a double wall cryogenic propellant tank with different insulations using one-dimensional flow over vertical plate approximation, Cryogenics 121 (2022), 103393.
[26] H. Scheufler, J. Gerstmann, Heat and mass transfer in a cryogenic tank in case of active-pressurization, Cryogenics 121 (2022), 103391.
[27] Z. Zuo, W. Jiang, X. Qin, Y. Huang, A numerical model for liquid–vapor transition in self-pressurized cryogenic containers, Appl. Therm. Eng. 193 (2021), 117005.
[28] Y. Zheng, P. Yang, Y. Liu, Q. Yang, C. Yan, X. Wang, Parametric optimization and analysis of thermodynamic venting system in liquid hydrogen tank under microgravity, Int. J. Hydrogen Energy 46 (2021) 40041–40053.
[29] R. Lv, Y. Huang, J. Wu, Thermodynamic analysis of partially filled hydrogen tanks in a wide scale range, Appl. Therm. Eng. 193 (2021), 117007.
[30] R. Farr, T. Sanders, RS-88 pad abort demonstrator thrust chamber assembly testing at NASA marshall space flight center, in: 41st AIAA/ASME/SAE/ASEE Joint Propulsion Conference & Exhibit, 2005, p. 4422. November-December 2003.
[31] M. Yoshida, T. Kimura, T. Hashimoto, S. Moriya, S. Takada, Overview of research and development status of reusable rocket engine, in: Chemical Rocket Propulsion, Springer, 2017, pp. 905–931.
[32] J.U. Brackbill, D.B. Kothe, C. Zemach, A continuum method for modeling surface tension, J. Comput. Phys. 100 (1992) 335–354.
[33] S.M. Ghiaasiaan, Two-phase Flow, Boiling, and Condensation: in Conventional and Miniature Systems, Cambridge University Press, 2007.
[34] R. Cox, The dynamics of the spreading of liquids on a solid surface. Part 1. Viscous flow, J. Fluid Mech. 168 (1986) 169–194.
[35] R.B. Bird, Transport phenomena, Appl. Mech. Rev. 55 (2002) R1–R4.
[36] D. Gueyffier, J. Li, A. Nadim, R. Scardovelli, S. Zaleski, Volume-of-fluid interface tracking with smoothed surface stress methods for three-dimensional flows, J. Comput. Phys. 152 (1999) 423–456.
[37] C.W. Hirt, B.D. Nichols, Volume of fluid (VOF) method for the dynamics of free boundaries, J. Comput. Phys. 39 (1981) 201–225.
[38] J.C. Li, H. Lin, K. Li, J.-F. Zhao, W.-R. Hu, Dynamic behavior in a storage tank in reduced gravity using dynamic contact angle method, Microgravity Sci. Technol. 32 (2020) 1039–1048.
[39] J.C. Li, H. Lin, J.-F. Zhao, K. Li, W.-R. Hu, Dynamic behaviors of liquid in partially filled tank in short-term microgravity, Microgravity Sci. Technol. 30 (2018) 849–856.
[40] W.H. Lee, A Pressure Iteration Scheme for Two-phase Modeling, Los Alamos Scientific Laboratory, Los Alamos, NM, 1979, pp. 79–975. Report No. LA-UR.
[41] S.C. De Schepper, G.J. Heynderickx, G.B. Marin, Modeling the evaporation of a hydrocarbon feedstock in the convection section of a steam cracker, Comput. Chem. Eng. 33 (2009) 122–132.
[42] D.L. Youngs, Time-dependent multi-material flow with large fluid distortion, in: In Numerical Methods for Fluid Dynamics, Academic Press, New York, 1982, pp. 273–285.
[43] S. Popinet, An accurate adaptive solver for surface-tension-driven interfacial flows, J. Comput. Phys. 228 (2009) 5838–5866.
[44] H. Dwyer, R. Kee, B. Sanders, Adaptive grid method for problems in fluid mechanics and heat transfer, AIAA J. 18 (1980) 1205–1212.